

# Comparison of High-Fidelity Turbulence Modelling Approaches for Hybrid CAA Studies of Trailing Edge Noise

Prakyath Pindi Nataraj\*

Technical University of Denmark, Frederiksborgej 399, 4000 Roskilde, Denmark

Franck Bertagnolio<sup>†</sup>, Niels Sørensen<sup>‡</sup> and Andreas Fischer<sup>§</sup>

Technical University of Denmark, Frederiksborgej 399, 4000 Roskilde, Denmark

Turbulence modelling approaches of different fidelity implemented in a three-dimensional incompressible Navier-Stokes solver are validated against DNS data from the literature for a channel flow characterized by a friction Reynolds number  $Re_\tau = 395$ . Wall-resolved large-eddy simulation (WRLES) and wall-stress modelled LES (WSMLES) are considered to obtain a precursor flow solution for a hybrid CFD-CAA simulation of turbulent boundary layer trailing-edge (TBL-TE) noise. A moderate Reynolds number case of the NACA4412 airfoil at an angle of attack of  $5^\circ$  is chosen for evaluating the applicability of these models. Validation of the flow solution for the airfoil simulations is done against direct numerical simulation (DNS) data from the literature. Based on the nature of the near-field aerodynamic data and spectra of wall-pressure fluctuations at locations near the trailing edge and its comparability with DNS, it is observed that the current WSMLES is more computationally efficient than WRLES. However, further work is required to make the combination of that and tripping by unsteady volume forcing give physically accurate results and render it suitable for precursor CFD simulations in hybrid CFD-CAA studies of turbulent boundary layer trailing edge noise in straight trailing-edge airfoils.

## I. Introduction

Turbulent boundary layer trailing edge (TBL-TE) noise has been experimentally proven by Oerlemans et al. [1] to be the primary source of broadband noise at design conditions in horizontal-axis wind turbines (HAWT). In practice, mitigation of wind-turbine noise is achieved by low-noise operation modes [2], whose development is done with the help of numerical noise prediction tools; furthermore, they are also required for certification purposes. Blade add-ons, in particular serrations, are also widely used to avoid a detrimental curtailment of annual energy production (AEP) that would ensue if low-noise operation modes were relied on for noise mitigation.

Empirical and semi-empirical [3–6] noise prediction models are mainstays in the industry owing to their fast turn-around times. But, their derivation is based on many simplifying assumptions regarding the geometry and flow physics that compromise their accuracy and limit their applicability. The validation of such models necessitates high-fidelity approaches that can handle complex flow physics and geometries. One such numerical approach is the hybrid CFD-CAA method, wherein a near-field incompressible/compressible flow solution from unsteady DNS, LES or hybrid RANS/LES computations is used as the precursor. From this precursor simulation, source terms based on the choice between analytical or numerical transport of the sound generated in the near-field to the far-field are computed. Some of the popular methods to obtain the predictions at an observer in the far-field are based on flow-acoustic splitting techniques [7, 8], analytical solutions of the Lighthill’s acoustic analogy equation [9–12] and the Boundary Element Method (BEM) [13].

Various authors have investigated the airfoil self-noise mechanism of TBL-TE noise in the purview of the design of low-noise airfoil profiles for wings, high-lift devices, wind turbine blades, and propellers. A number of them have resorted to the hybrid CFD-CAA method. Shen et al. [14] utilized a splitting technique in which Tenaud et al. [15]’s mixing scale model is used to model the turbulent eddy-viscosity. Good agreement with experimental data was observed for the low angle of attack cases of an isolated airfoil. However, the aerodynamic validation was limited to comparing

\*PhD Student, Department of Wind and Energy Systems, E-mail: prakpn@dtu.dk

<sup>†</sup>Senior Researcher, Department of Wind and Energy Systems

<sup>‡</sup>Professor, Department of Wind and Energy Systems

<sup>§</sup>Senior Researcher, Department of Wind and Energy Systems

the time-averaged integral coefficients alone at low Reynolds numbers. Wang et al. [16] performed incompressible LES of a CD airfoil whose span was a tenth of the chord. The effect of the sub-grid scales was modelled by Lilly's dynamic subgrid-scale model [17]. The chord-based Reynolds number was  $1.5 \times 10^5$ , considered a low Reynolds number flow regime. Aerodynamic validation of the precursor CFD solution was conducted against experimental data from an open-jet anechoic wind tunnel test campaign. The LES domain was embedded in a RANS solution field, which included the nozzle and jet geometries; this was done to account for the nozzle-jet interaction, which is prominent in open-jet wind tunnels. Accurate comparisons were observed between the mean surface pressure coefficient and wake velocity profiles. The wall pressure spectra at different chordwise sections near the trailing edge in the experiment and simulation found good agreement. The decay of the spanwise correlation to negligible values for spanwise separation of half the span or more ratified the choice of a reduced span in the simulations. Wolf et al. [18] carried out compressible LES simulations of an isolated NACA0012 profile at transitional Reynolds numbers of about  $4 \times 10^5$ . Similar to earlier literature, an airfoil span of a tenth of the chord was considered. Zero and non-zero angles of attack were considered, along with clean and tripped pressure side surfaces. The non-dimensional mean velocity profiles in the viscous sublayer agreed, unlike the log-law region, where a mismatch existed. The boundary layer profiles, wake velocity profiles, and the simulation's spectra of wall pressure fluctuations (wall PSD) matched experimental trends for both the cases of tripped and clean pressure side surfaces. At a point near the pressure-side trailing edge for the clean case, a tone corresponding to vortex-shedding caused by the laminar boundary layer was also captured in the wall pressure spectrum plot. Upon inspecting the far-field SPL spectrum for airfoils with tripped suction and pressure sides, the presence of harmonic tones indicated vortex shedding due to a blunt trailing edge, which was then confirmed by flow visualization. The phenomenon is expected as the bluntness parameter [19] exceeded the threshold of 0.3.

The combination of airfoil self-noise mechanisms contributing to the noise generated at low, moderate and high Reynolds are distinct [20]. Consequently, the data from low and moderate Reynolds number numerical and experimental studies is not representative of the high Reynolds numbers characteristic of the outer 30% of the blade of a MW-size wind turbine, which is responsible for the aerodynamic noise emissions. This study is part of an ongoing internal project aiming to develop the necessary numerical simulation tools that enable accurate noise predictions for the trailing edge noise emissions of straight and serrated trailing-edge thin airfoils. Only hybrid CFD-CAA approaches will be explored as they are computationally feasible. As a first step in achieving the project's objectives, the high-fidelity turbulence modelling capabilities in EllipSys3D [21] are validated with the channel flow DNS data from Moser et al. [22] and the cambered-airfoil DNS data from Hosseini et al. [23]. In the scope of this study are two eddy viscosity sub-grid-scale model-based WRLES and WSMLES approaches, which are explained in-brief in the following section. Subsequently, their evaluation with respect to DNS will be based on comparing the near-field aerodynamic data such as mean surface pressure coefficient distribution, wall-pressure spectra, boundary layer velocity profiles, boundary layer thickness, etc. In doing so, it will be elucidated on whether the current WSMLES method is suitable for capturing the noise-generating near-field turbulence.

The near-field flow solution obtained in this study will be used as a precursor CFD solution in conjunction with an acoustics solver to predict the far-field noise; this, however, will be the focus of a follow-up study where this approach will also be validated against experimental data from a high Reynolds number airfoil test campaign. A comprehensive experimental campaign has been carried out at the Poul La Cour wind tunnel (PLCT) at the Technical University of Denmark (DTU) to characterize the high Reynolds number TBL-TE noise from straight-TE and serrated NACA 63-018 airfoils sections [24]. The resulting data will be used as a reference to validate the existing CFD-CAA tools and noise prediction models [25, 26].

## II. Methodology

The near-field flow solution is computed with the incompressible flow solver EllipSys3D [21, 27, 28] developed in-house at the Technical University of Denmark. EllipSys3D is a parallelized multiblock solver capable of handling steady and unsteady flow problems governed by the incompressible Navier Stokes equations, which are discretized on the cell centers by the finite volume method. Temporal discretization is achieved by the second-order dual time-stepping method. The solver entails turbulence modelling approaches of different fidelities ranging from the lower-fidelity RANS/URANS to high-fidelity wall-resolved LES. An overview of the turbulence modelling approaches relevant to this study is given below.

In LES, the energy-containing eddies/large scales are resolved, and the sub-grid scales are modelled. The filtered Navier Stokes equations that govern the resolved flow are:

$$\frac{\partial \bar{u}_i}{\partial x_i} = 0 \quad (1)$$

$$\frac{\partial \bar{u}_i}{\partial t} + \frac{\partial (\bar{u}_i \bar{u}_j)}{\partial x_j} = -\frac{\partial \bar{p}}{\partial x_i} + \nu \frac{\partial^2 \bar{u}_i}{\partial^2 x_i} + \frac{\partial \tau_{ij}}{\partial x_j} \quad (2)$$

In the above equations, the variables with "-" are the filtered primitive variables, with  $u_i$  being the velocity,  $p$  the pressure,  $\nu$  being the kinematic viscosity and  $\tau_{ij}$  the sub-grid stress tensor. The sub-grid stress tensor is a composition of the tensors of the Leonard stress, cross-stresses and the sub-grid Reynolds stress. The expression for the same is given below:

$$\tau_{ij} = \bar{u}_i \bar{u}_j - \bar{u}_i \bar{u}_j = \left( \bar{u}_i \bar{u}_j - \bar{\bar{u}}_i \bar{\bar{u}}_j \right) - \left( \bar{\bar{u}}_i u'_j + u'_i \bar{\bar{u}}_j \right) - \bar{u}'_i \bar{u}'_j \quad (3)$$

The variable  $u'_i$  refers to the sub-grid velocity, which is defined as  $u'_i = u_i - \bar{u}_i$ . Equation 4 corresponds to the eddy viscosity model, which is one of the approaches to model the sub-grid stress tensor.

$$\tau_{ij} = \nu_t \left( \frac{\partial \bar{u}_i}{\partial x_j} + \frac{\partial \bar{u}_j}{\partial x_i} \right) - \frac{2}{3} k \delta_{ij} \quad (4)$$

In the above equation,  $\nu_t$  and  $k$  denote the eddy viscosity and the sub-grid turbulent kinetic energy, respectively. The wall-resolved approach considered in the current study used the WALE [29] sub-grid scale model. An algebraic wall-stress model based on the WALE model is also used.

### A. WALE model

Nicoud and Ducros [29] proposed the WALE model (Eq. 5) with the objective of defining the eddy viscosity as the function of an operator that could be applicable on any grid types, that is a function of both the strain and rotation rate tensors, and that produces near-zero values in the vicinity of a wall.

$$\nu_t = (C_w \Delta)^2 \frac{\left( S_{ij}^d S_{ij}^d \right)^{3/2}}{\left( \bar{S}_{ij} \bar{S}_{ij} \right)^{5/2} + \left( S_{ij}^d S_{ij}^d \right)^{5/4}} \quad (5)$$

In Eq. 5,  $\bar{S}_{ij}$  is the strain rate tensor,  $\Delta$  is the sub-grid length scale. The model constant  $C_w$  in the current channel flow simulations is fixed at 0.5. The expression for the tensor  $S_{ij}^d$  is given by Eq. 6; here,  $\bar{g}_{ij}$  is the velocity gradient tensor.

$$S_{ij}^d = \frac{1}{2} \left( \bar{g}_{ij}^2 + \bar{g}_{ji}^2 \right) - \frac{1}{3} \delta_{ij} \bar{g}_{kk}^2 \quad (6)$$

### B. Algebraic Wall Stress Model

The algebraic wall-stress model involves defining a matching distance  $h_{wm}$  above the wall. The velocity  $u_{||}(h_{wm})$  tangential to the wall at this location computed on the LES grid is used to estimate the local friction-velocity ( $u_\tau$ ) by iteratively solving a model for the boundary layer velocity by the Newton-Raphson method. The wall-friction  $\tau_w = \rho u_\tau^2$  is thus computed and enforced in the solver.

The boundary layer velocity profile assumed here is Reichardt's model [30], given in Equation 7. Here, the model constants are the Von Kármán constant  $\kappa = 0.4$ ,  $C = 7.4907$ ,  $B_1 = 11$  and  $B_2 = 3$ .

$$u^+ = \frac{1}{\kappa} \left( 1 + \kappa y^+ \right) + C \left( 1 - e^{-\frac{y^+}{B_1}} - \frac{y^+ e^{\frac{-y^+}{B_2}}}{B_1} \right) \quad (7)$$

### C. Tripping by random volume forcing

In the airfoil simulations, tripping on the suction and pressure sides is achieved by applying an unsteady random volume force in the wall-normal direction. The volume force ( $F_2$ ), which is used as a source term in the incompressible Navier Stokes equations, is formulated by Schlatter and Örlu [31] as follows:

$$F_2 = \exp\left(\left[\left(x - x_0\right)/\ell_x\right]^2 - \left[y/\ell_y\right]^2\right) g(z, t) \quad (8)$$

In the above equation,  $x_0$  is the streamwise position of the tripping force,  $\ell_x$  and  $\ell_y$  are the streamwise and wall-normal extent of the volume force, which has a gaussian shape. The spanwise ( $z$ ) and temporal variation of the volume force  $g(z, t)$  is given by Equation 9, where  $b(t) = 3p^2 - 2p^3$ ,  $p = t/t_s - i$  and  $i = \text{int}(t/t_s)$ , the function  $\text{int}()$  provides an integer as the output to the input argument, and  $h^i(z)$  is a random harmonic signal which has a unit amplitude for wavenumbers below  $2\pi/z_s$  and zero for those above it.  $z_s$  is the cut-off length in the spanwise direction.

$$g(z, t) = A_t \left[ \{1 - b(t)\} h^i(z) + b(t) h^{i+1}(z) \right] \quad (9)$$

According to this definition of the volume force, for a given location of the tripping line,  $t_s$ ,  $z_s$ ,  $\ell_x$ , and  $\ell_y$  are the important input parameters.

## III. Results and Discussion

### A. Channel Flow Test Case

#### 1. Test Case Description

The data from the DNS turbulent channel flow test case of Moser et al. [22] is used in the present study to validate the aforementioned turbulence modelling approaches in EllipSys3D. The channel flow is characterized by a friction Reynolds number  $Re_\tau = u_\tau H/\nu = 395$ , where  $u_\tau$  is the friction velocity and  $H$  is the channel half-height. The bulk Reynolds number is  $Re_b = U_b 2H/\nu = 13800$ , where  $U_b$  denotes the bulk flow velocity considered to be 1m/s.

#### 2. Computational Domain and SImulation Setup

The channel considered in the current simulation has dimensions  $L_x \times L_y \times L_z = 2\pi \times \pi \times 2$  with the Cartesian  $z$  direction being the wall-normal direction (and  $H = 1m$ ). The transverse boundaries are assumed to be no-slip walls. Periodicity is enforced on both the streamwise and spanwise faces to emulate flow between two semi-infinite flat plates. The grids used in the current validation study are listed in Table 1. The domain is discretized into a cartesian grid with uniform streamwise and spanwise spacing. In the WRLES grids, the wall-normal ( $z$ ) cell size distribution follows a hyperbolic sine distribution. For the WSMLES grids, a matching distance of  $h_{wm} = 0.1H$  is chosen to evaluate the wall friction. This near-wall region is resolved by five cells of the same size with  $\Delta z_w^+ \approx 7.9$ . Beyond the matching distance, the cell size distribution follows a hyperbolic sine distribution. For the sake of brevity, the near-wall region is referred to as the wall-modelling layer; this is not to be confused with the conventional definition of the wall-modelling layer, where governing equations for equilibrium or non-equilibrium wall-stress models are solved on an overlapping grid. An inaccurate prediction of flow and stress profiles in this region is natural owing to the poor resolution.

Case	$N_x \times N_y \times N_z$	$\Delta x^+$	$\Delta y^+$	$\Delta z_w^+$	$\Delta z_c^+$	$\Delta t^+$	CFL
DNS Moser [22]	$256 \times 193 \times 192$	10.00	6.5	N/A	4.40	N/A	N/A
WRLES Grid 1	$256 \times 128 \times 128$	9.69	9.69	0.81	13.33	0.23	0.47
WRLES Grid 2	$64 \times 128 \times 96$	38.77	9.69	0.83	19.11	0.56	0.29
WSMLES Grid 1	$128 \times 64 \times 64$	19.39	19.39	7.90	16.67	0.45	0.29
WSMLES Grid 2	$64 \times 64 \times 64$	38.77	19.39	7.90	16.67	0.45	0.29

Table 1 Grids used for the channel flow validation.

On WRLES Grid 2, a time-step sensitivity study was conducted as recommended by Choi and Moin [32] and it was found that an accurate flow solution is obtained at a non-dimensional time-step of  $\Delta t^+ = \Delta t u_\tau^2 / \nu = 0.56$ . For WRLES Grid 1 and both the WSMLES grids, the choice of time-step was based on the temporal resolution that would be required to resolve the velocity profiles on a given grid while having a CFL number below unity. To accelerate the transition of the flow to turbulence in the WRLES grids, the flow solution is initiated by a laminar flow profile overlaid by streak-like structures as formulated in Schoppa and Hussain [33]. This flow initialization in the WSMLES simulations resulted in false shear stress prediction; it was found that using the flow solution from WRLES Grid 1 for initialization remedied the issue. A PID controller is used in all the channel flow simulations to enforce constant mass flux in the domain; it also enables faster transition to turbulence compared to the specification of a constant pressure gradient [34]. Convective terms in the governing equations are discretized by the fourth-order central differencing scheme. Temporal discretization is achieved by a second-order three level implicit method. An initial transient amounting to about 95 flow-through times is neglected.

### 3. Results

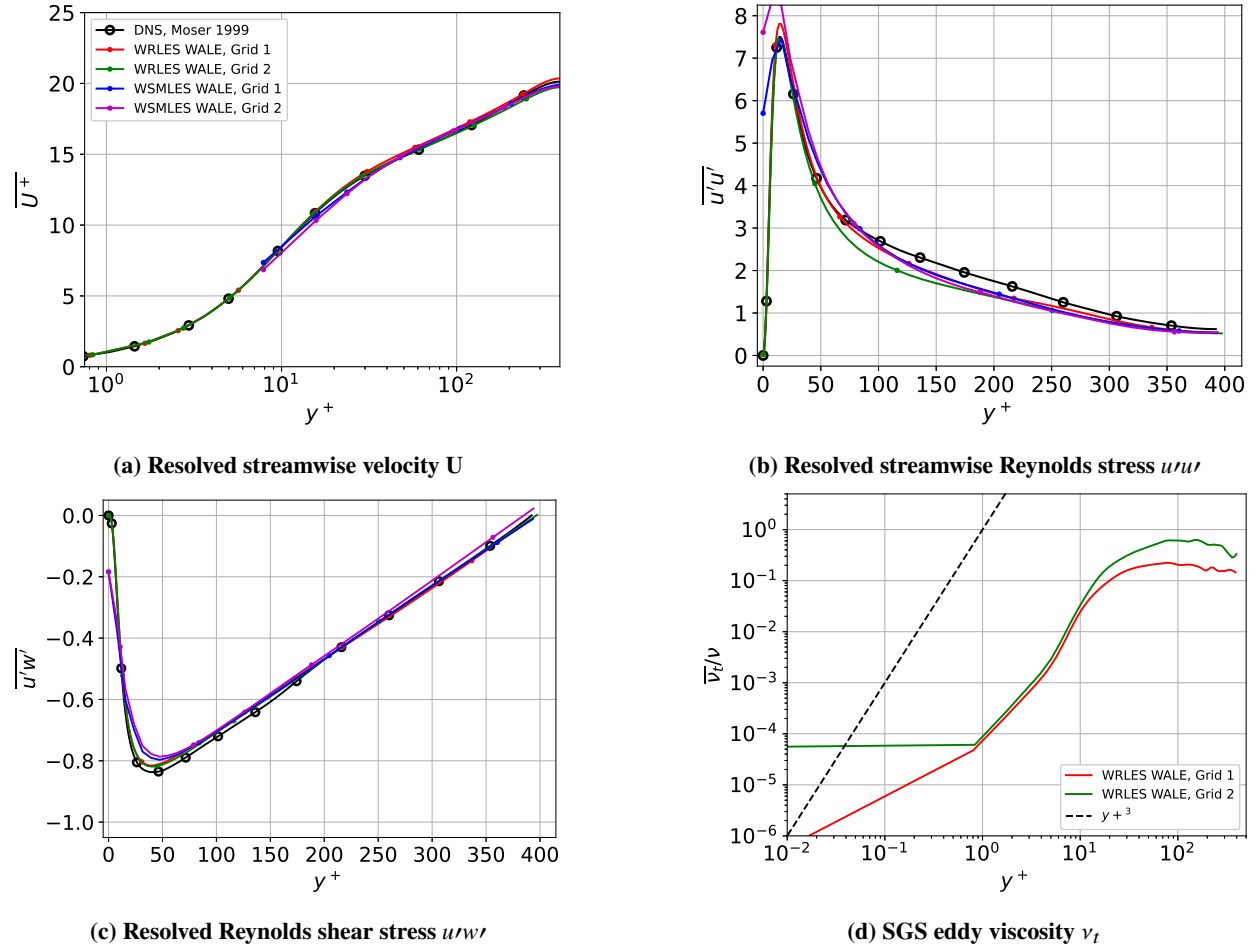


**Fig. 1 Comparison of the wall-normal variation of time and horizontally averaged profiles of a few non-dimensional quantities against DNS data of Moser et al. [22].**

Profiles normalized in wall-units are plotted in Figure 1; they correspond to those obtained by time and horizontal averaging of the flow solution in the wall-parallel directions for 150 flow passes for both WRLES and WSMLES. The overbar refers to the averaged quantities. It is seen in Figure 1a that the normalized mean streamwise velocity  $\bar{u}^+$  in the sub-layer is in good agreement with the DNS data in both linear and log-law regions for both WRLES and WSMLES approaches. In Figure 1b, the normalized wall-distance of the peak in the profiles of the streamwise resolved

Reynolds stresses  $\overline{u'u'}$  for the WRLES grids match that of the reference. The profiles of the same at the core, although underpredicted collapse except for that from WRLES Grid 2, which is due to a relatively coarse spatial resolution in the core region. The plot in Figure 1c shows that both the approaches resolve most of the cross-stresses  $\overline{u'w'}$ ; the total cross-stresses (not shown here) nearly overlaps with the DNS data throughout the domain. The plot of the non-dimensional eddy-viscosity depicts the  $y^{+3}$  of the WALE model consistent with the observations of Nicoud et al. [29].

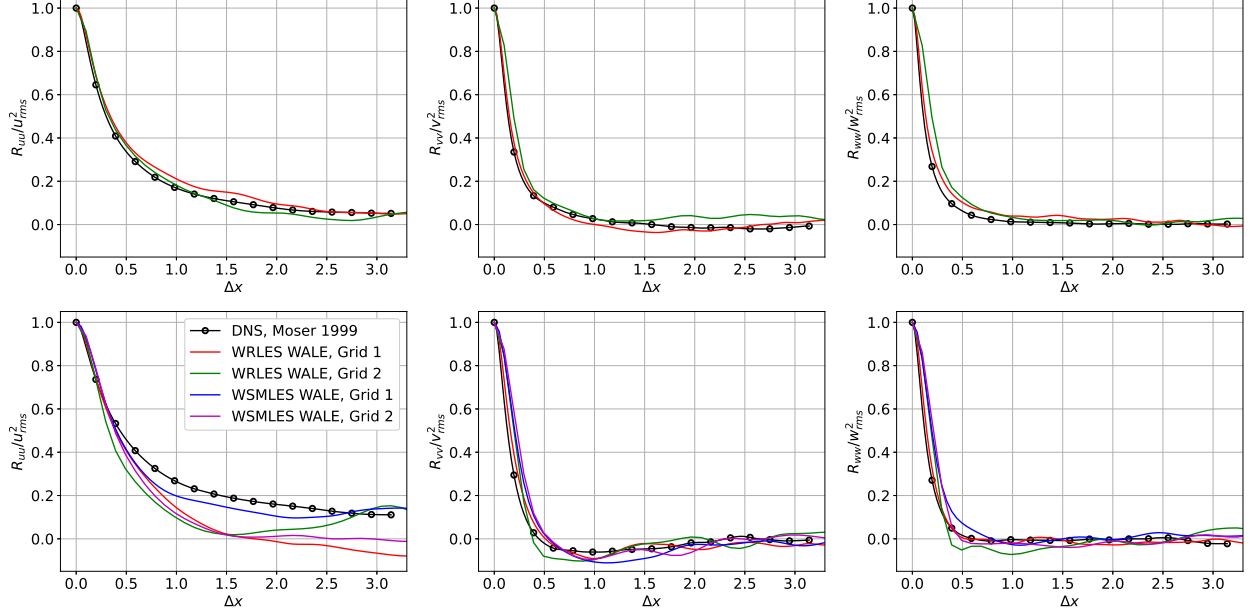


**Fig. 2 Comparison of normalized two-point correlation of fluctuating velocities  $u'$ ,  $v'$  and  $w'$  at  $y^+ \approx 19$  (above) and  $y^+ \approx 200$  (below) against the DNS reference data.**

The normalized streamwise two-point correlation in Figure 2 is plotted at two wall-normal locations. The results from the WSMLES are not included at the location  $y^+ \approx 19$  as it lies below the matching distance, where the LES solution is inaccurate due to poor resolution. The good agreement of both the WRLES simulations against DNS in this region can be attributed to the clustering of cells close to the wall because of the hyperbolic sine distribution. Furthermore, since this region is in the vicinity of the wall and the flow is characterized by a low friction Reynolds number, the energy-containing eddies near the wall are relatively large and, thus, are well-resolved on coarse grids. At  $y^+ \approx 200$ , the streamwise two-point correlations of both  $v'$  and  $w'$  show good agreement between the simulations and also with DNS. It is interesting to note that in the two-point correlation plot of the streamwise fluctuations, the WSMLES WALE Grid 1 simulation agrees the best with DNS. It is contrary to the expectation that the two-point correlation function would have exhibited larger values with grid coarsening; this and an abrupt increase in the value of the two-point correlation on the WRLES Grid 2 simulation could also indicate that the simulation should be run longer to reach a statistical stationary state. For each of the simulations, the plots of the normalized two-point correlation in the spanwise direction show little discrepancy between each other and the DNS reference; they are thus not shown here for brevity.

The streamwise and spanwise wavenumber spectra of turbulent kinetic energy (TKE) plotted in Figure 3 show that the energy of the TKE signal is consistent with that of the DNS for all the simulations until a certain wavenumber, at which the scales seem to attenuate and the energy of the TKE drops until it reaches the minimum at the grid-based cut-off wavenumber.

In Figure 4, the normalized two-point correlation of wall pressure is plotted for all the channel flow simulations. The general trend observed is that in the coarser of the two WRLES or WSMLES, the wall-pressure fluctuations are correlated for a relatively longer streamwise or spanwise separation. The same can be corroborated by comparing the integral lengthscales given in Table 2. It is noticed here that although both the WRLES grids have the same spanwise resolution, the grid that is coarser in the streamwise and wall-normal direction resolves scales which would be larger in comparison with the fine grid as the coarse resolution limits the turbulence cascade process.

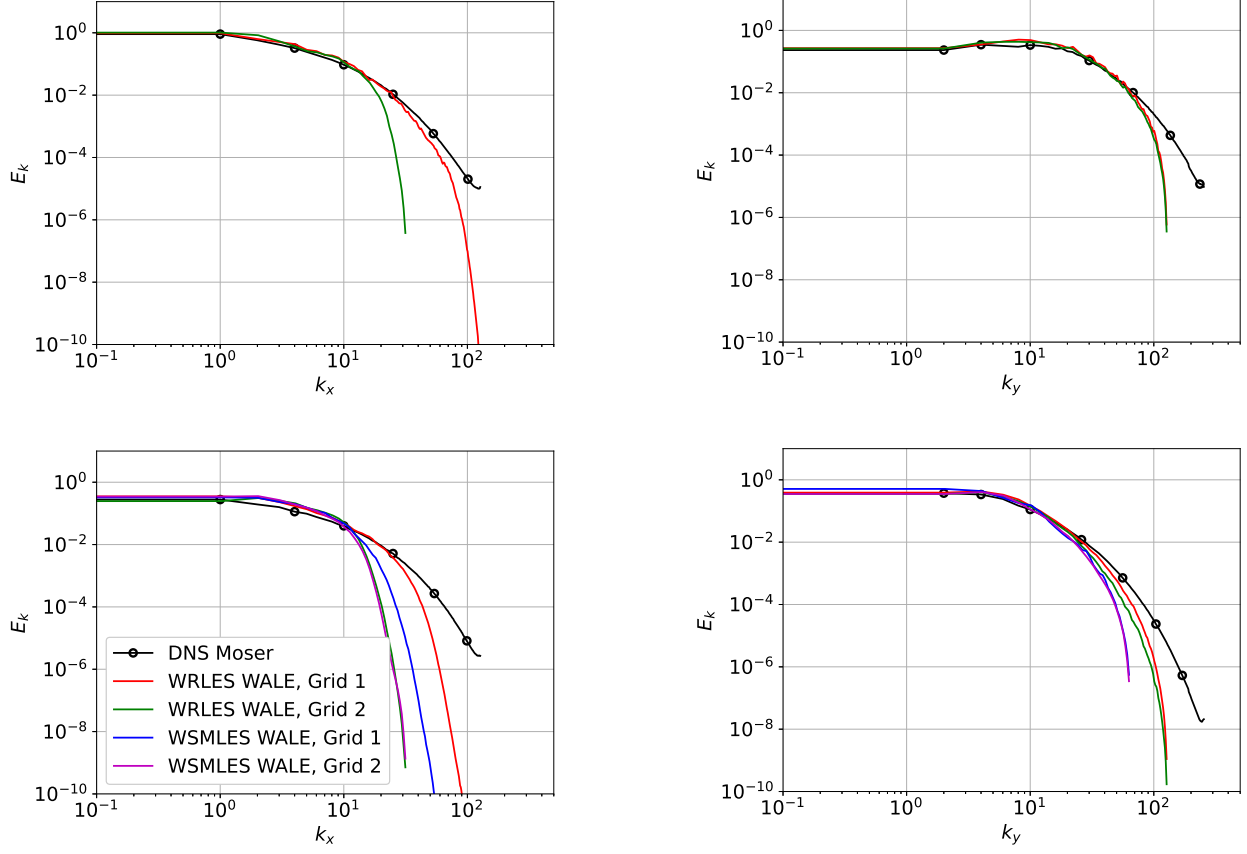


**Fig. 3** Comparison of the streamwise and spanwise wavenumber spectra of the turbulent kinetic energy at  $y^+ \approx 19$  (above) and at  $y^+ \approx 200$  (below) against DNS data of Moser et al. [22].

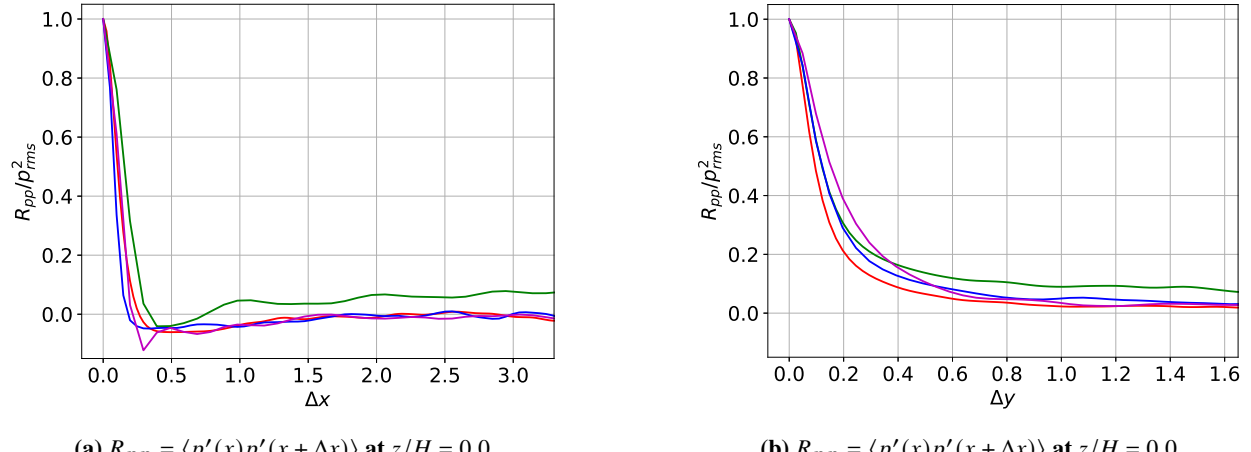


**Fig. 4** Comparison of the normalized two-point correlation of wall-pressure  $p'$  along the streamwise and spanwise directions.

Case	$L_{pp_x}/H$	$L_{pp_y}/H$
WRLES Grid 1	0.1126	0.1627
WRLES Grid 2	0.1565	0.2364
WSMLES Grid 1	0.0793	0.1798
WSMLES Grid 2	0.1106	0.2328

**Table 2 Integral length scale of the wall-pressure fluctuations in the streamwise and spanwise directions.**

## B. NACA 4412 Test Case

### 1. Test Case Description

As stated earlier, the ongoing study aims to assess the applicability of the WSMLES approach to resolve the near-field flow physics relevant to the TBL-TE noise mechanism. In this regard, this section corresponds to the aerodynamic validation of the near-field flow solution against the DNS data from Hosseini et al. [23]. The flow parameters relevant to this case are given in Table 3. Both suction and pressure side boundary layers are tripped at the chordwise location  $x/c = 0.1$ .

Parameter	Value
Chord-based Reynolds number ( $Re_c$ )	$4.00 \times 10^5$
Chord length ( $c$ )	1 m
Angle of attack ( $\alpha$ )	5.00°
Freestream Velocity ( $U_\infty$ )	5.92 m/s

**Table 3 Flow parameters of the considered airfoil validation test case.**

### 2. Computational domain and simulation setup

For the airfoil simulations, a body-fitted, block-structured, pseudo 2D O-grid is used. The domain has a radius of  $20c$ . A fractal topology is used to localize the clustering of elements to the vicinity of the airfoil. Furthermore, it also helps maintain the domain size large enough so that the effect of the induced velocity is accounted for, thereby minimizing the discrepancy between the geometric and effective angle of attack.

The baseline 2D O-mesh is generated by the hyperbolic grid-generation tool HypGrid2D [35]. The flow solution from a 2D RANS simulation of the same case serves as the basis for designing the LES grids. Based on the prediction of the friction coefficient  $C_f$  on the airfoil, the chordwise distribution of elements is made such that  $\Delta x^+ \leq 40$  and  $\Delta z^+ \leq 20$ ; here,  $x$  refers to the direction tangential to the airfoil surface and  $z$  is the spanwise direction. The size of the first cell in the wall-normal ( $y$ ) direction  $\Delta y_w^+ \leq 0.8$  throughout the chordwise extent on the WRLES grid and  $\Delta y_w^+ \leq 20$  throughout the chordwise extent on the WSMLES grid. The fractal grid consists of a pseudo2D O-grid encompassing the airfoil. Fractal layers are then built upon this pseudo2D region by reducing the number of spanwise blocks towards the outer boundaries. The extent of the pseudo2D region in the wall-normal direction is  $1.5 * \delta_{99}$  ( $x/c = 0.98$ ); here,  $\delta_{99}$  corresponds to the 99% boundary layer thickness, which is estimated from the baseline 2D RANS solution. A hyperbolic tangent distribution is used to fix the cell size in the wall-normal direction such that adequate clustering is ensured close to the airfoil. The boundary layer thickness at  $x/c = 0.98$  on the suction side of the airfoil is considered such that the underlying boundary layer turbulence near the trailing edge (responsible for TBL-TE noise) is resolved. The spanwise extent  $L_z$  of the domain is about  $2.6 * \delta_{99}$ . Figure 5 shows the cross-section of the domain in which the fractal layers in the WRLES and WSMLES grids can be seen. The figure only depicts the distribution of the blocks in the domain. More information about the grid parameters is given in Table 4.

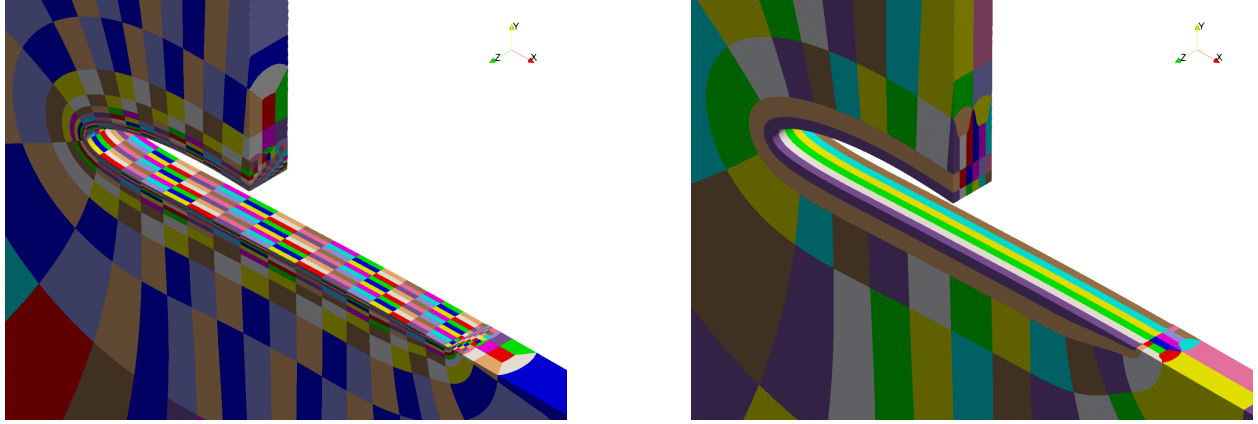


**Fig. 5** Distribution of blocks in the domain depicting the fractal topology used for the WRLES (left) and the WSMLES (right) grids.

Case	$N_{cells}$	$N_x$	$N_y$	$N_z$	$N_{y\_pseudo2D}$	$N_{fractals}$	$N_{cells}/block$	$\Delta y_w^+$
WRLES	$\sim 154.40 \times 10^6$	1216	640	288	352	4	$32^3$	$\leq 0.8$
WSMLES	$\sim 77.41 \times 10^6$	1200	336	288	96	2	$48^3$	$\leq 20$

**Table 4** Details of the WRLES and WSMLES fractal grids.

Since the friction Reynolds number ( $Re_\tau$ ) close to the leading edge on the suction side is about 25, the first grid point off the wall is used to evaluate the wall friction as per Equation 7.

The airfoil surface is assumed to be a no-slip wall, and periodicity is enforced on the spanwise faces. A convective boundary condition is imposed on a sector of the outflow boundary downstream of the airfoil, which has an arc angle of  $176^\circ$ . The remaining part of the outer boundary corresponds to the laminar inflow boundary condition. Spatial discretization is achieved by a fourth-order central differencing scheme, which is modified to include an artificial dissipation term to ensure stability. The solution is advanced in time by a second-order three level implicit method. About 25 flow-through times are completed before the simulation data is recorded for 4 flow-through times on both the WRLES and WSMLES cases. For the WRLES simulation, a non-dimensional timestep of  $1.48 \times 10^{-4} * c/u_\infty$  corresponding to a CFL number of 0.5 is used; the same for the WSMLES simulation is  $2.96 \times 10^{-4} * c/u_\infty$  and 0.5 respectively.

### 3. Particulars of Tripping

Both Schlatter and Örlü [31] and Hosseini et al. [23] prescribe the parameters based on the local laminar boundary layer displacement thickness  $\delta^*$ ; the streamwise extent of forcing  $l_x = 4\delta^*$ , wall-normal extent  $l_y = \delta^*$ , temporal cut-off scale  $t_s = 4\delta^*/U_\infty$  and spanwise cut-off scale  $z_s = 1.7\delta^*$ . The same spanwise and temporal cut-off scales were used for the current WMLES and WSMLES simulations. However, a relatively coarser resolution in the chordwise direction required the usage of a wider gaussian distribution of the volume forcing term. The spanwise extent was chosen such that the gaussian was distributed over four cells, resulting in an  $l_x = 6.56\delta^*$  and  $l_x = 10.07\delta^*$  on the suction and pressure sides. The wall-normal extent  $l_y$  used in the WRLES is the same as the prescribed value, whereas  $l_y = 2.83\delta^*$  on the suction side and  $l_y = 3.24\delta^*$  on the pressure side. The wall-normal extent in the WSMLES simulation is chosen in such a way that it covers two cells in the wall-normal direction.

### 4. Validation of the near-field flow solution

The plots of time and horizontal averaged pressure coefficient shown in Figure 6 from both the LES methods nearly overlap with the baseline 2D RANS simulation that was used for generating the grids and also the DNS reference of Hosseini et al. [23]. In the plot comparing the distribution of the friction coefficient  $C_f$ , a consistent behaviour in the laminar region is noticed on both the pressure and suction sides. Deviations from the DNS reference can be attributed to

the local airfoil surface grid that is used. Due to the tripping at  $x/c = 0.1$ , a peak in  $C_f$  is observed on both the suction and pressure sides on all the simulations, following which it drops gradually to a minimum near the trailing edge for the suction side in the WRLES simulation. Unlike the DNS reference, there is no subsequent drop in  $C_f$  followed by a secondary peak after the tripping location on the suction side; this implies bypass transition of the boundary layer on the suction side. In the WSMLES, a small drop in  $C_f$  is noticed just downstream of the tripping location; this is followed by a secondary peak at  $x/c \approx 0.3$  where the transition of the boundary layer to turbulence occurs. The value of suction-side  $C_f$  in the WSMLES is consistently overpredicted following the tripping location, which is also followed in the WRLES simulation after  $x/c = 0.7$ . This could be an indicator that the amplitude of volume forcing on the suction side is higher relative to the reference. On the pressure side, the  $C_f$  predicted from both WRLES and WSMLES drop to laminar values. A secondary peak denoting the transition location can be identified at  $x/c \approx 0.4$  and at  $x/c \approx 0.7$  for the WRLES and WSMLES simulations. Downstream of the transition location, the friction coefficient predicted is identical to that obtained from 2D RANS and also the DNS reference.

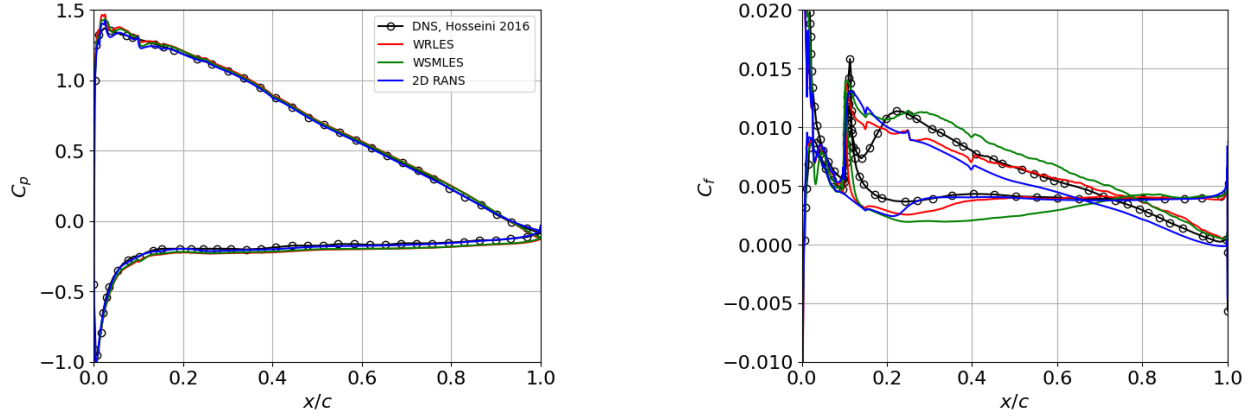


**Fig. 6 Time and horizontal averaged pressure coefficient  $C_p$  (left) and skin-friction coefficient ( $C_f$ ) comparison between (red) WRLES, (green) WSMLES and 2D RANS (blue)**

The Q-criterion contour plots in Figure 7 and Figure 8 help visualize the flow development downstream of the trip location. In Figure 7a, hairpin-like vortices are seen developing immediately after the volume forcing line, corroborating the behaviour of  $C_f$  in this region that was discussed earlier. These structures are absent at the tripping location in the WSMLES simulation. However, certain hairpin-like structures do appear further downstream, where the transition of the boundary layer is likely to occur as per the plot of  $C_f$  distribution in Figure 6. A relatively coarse grid resolution in the WSMLES simulation could be causing this delay.

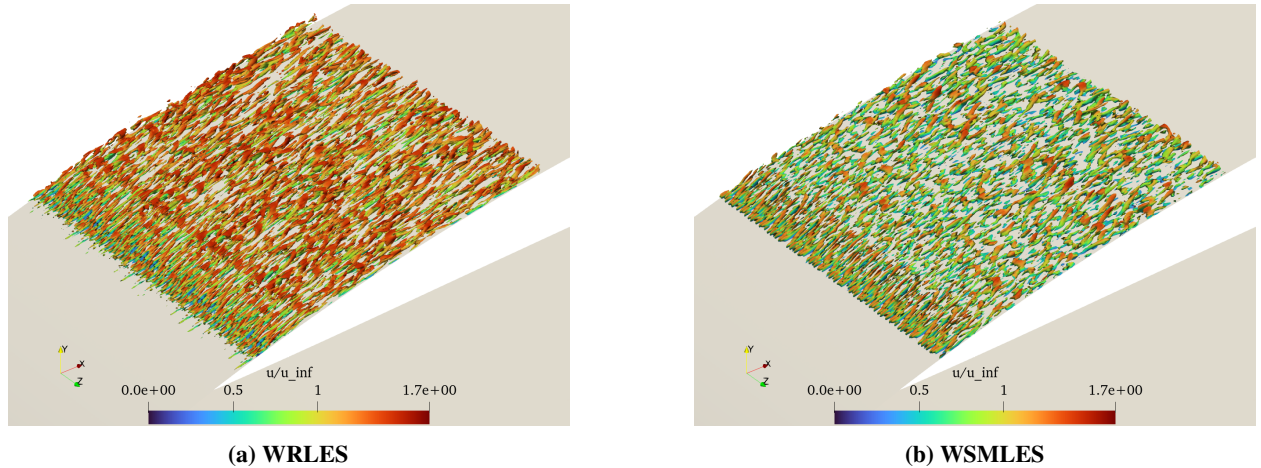


**Fig. 7 Isosurfaces of Q-criterion ( $Q = 4 \times 10^5$ ) colored by normalized streamwise velocity ( $u/u_\infty$ ) at  $x/c = 0.1$  on the suction side.**

The Q-criterion plots in Figure 8 on the pressure side show that the volume forcing used presently is unable to help transition the boundary layer to a turbulent one in its downstream vicinity as the instabilities triggered by volume forcing are dampedened due to flow relaminarization.

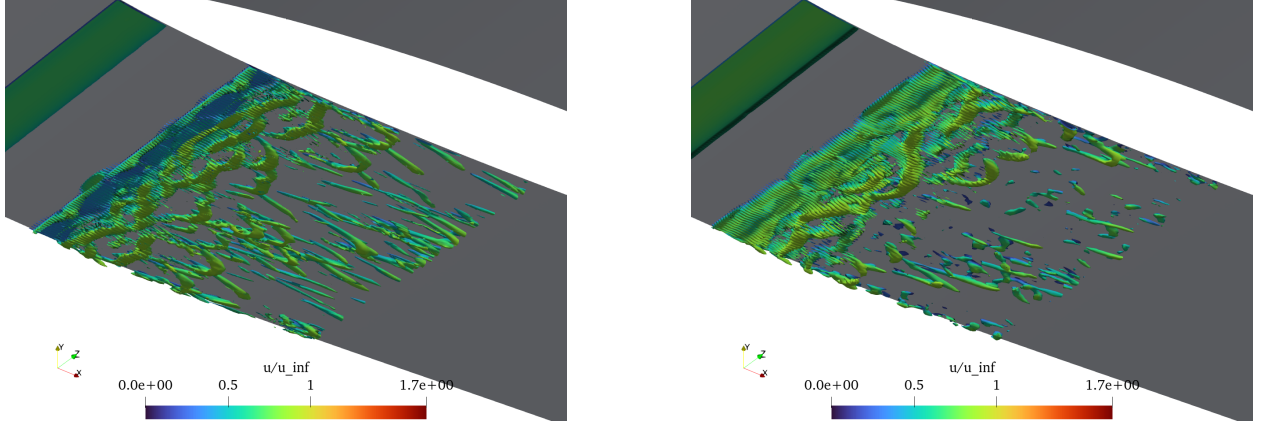


**Fig. 8** Isosurfaces of Q-criterion ( $Q = 3.5 \times 10^4$ ) colored by normalized streamwise velocity ( $u/u_\infty$ ) at  $x/c = 0.1$  on the pressure side for WRLES (left) and WSMLES (right).

Since the boundary layer develops over an adverse pressure gradient on the suction side as opposed to a favourable pressure gradient on the suction side, the suction side boundary layer is expected to grow faster relative to that on the pressure side. This phenomenon is natural for airfoils at non-zero angles of attack; the behaviour is more pronounced with cambered airfoils; the same is observed in the plots of the different boundary layer thickness definitions in Figure 9. The discrepancy between the DNS and present simulations in terms of the displacement thickness  $\delta^*$  and momentum thickness  $\theta$  on the pressure side arises due to the boundary layer transitioning much later than  $x/c = 0.1$ . As a consequence, they are underpredicted through the whole chord. On the suction side, the development of the displacement thickness in the WRLES case is nearly identical to that of the DNS, unlike that in WSMLES. The relative over-prediction of the suction-side momentum thickness is consistent with the overpredicted friction coefficient  $C_f$  downstream of the suction side trip seen earlier in Figure 6.

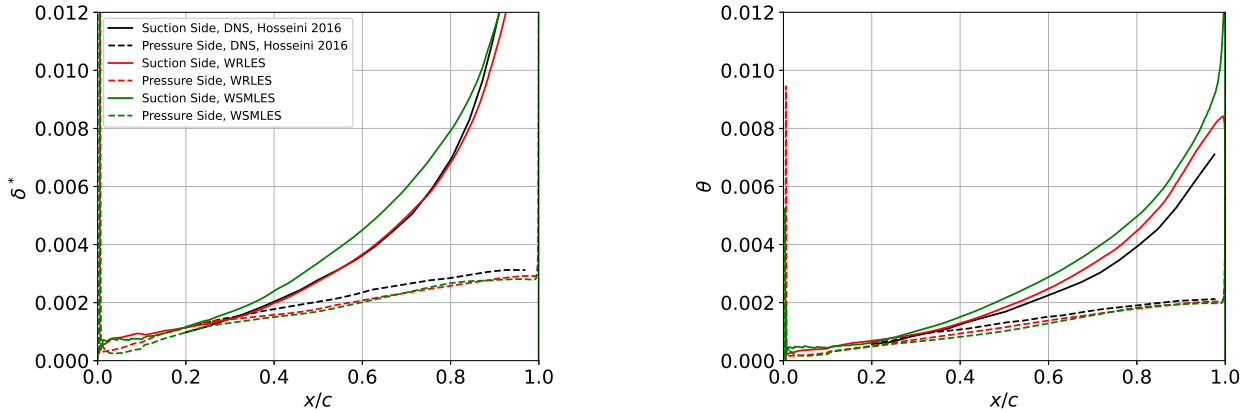


**Fig. 9** Chordwise variation of the time and horizontal averaged boundary layer displacement thickness  $\delta^*$  (left) and momentum thickness  $\theta$  (right) for the (red) WRLES and (green) WSMLES flow solution.

In Figure 10, the non-dimensional profiles of the velocity tangential to the airfoil are compared. The profiles for the WRLES simulations follow the general trend where the effect of the adverse pressure gradient is seen with the increased velocity in the wake region on the suction side. The comparison between the pressure and suction side boundary layers is not equivalent as they are not at the same  $Re_\tau$ . The log-law region on the suction and pressure sides has an intercept different from that of theory and the DNS reference. This could be attributed to the inadequate grid resolution as a

$\Delta x^+ \approx 40$  is typical for coarse WRLES simulations. In the WSMLES case at  $x/c = 0.65$ , the velocity profile on the pressure side does not resemble a turbulent profile because the boundary layer is yet to transition to turbulence. The incorrect log-law intercepts in both Figure 10a and Figure 10b could be a result of both coarse resolution and incorrect prediction of the local wall-friction ( $\tau_w$ ). Further analysis should be carried out to conclusively arrive at the cause of these erroneous profiles.

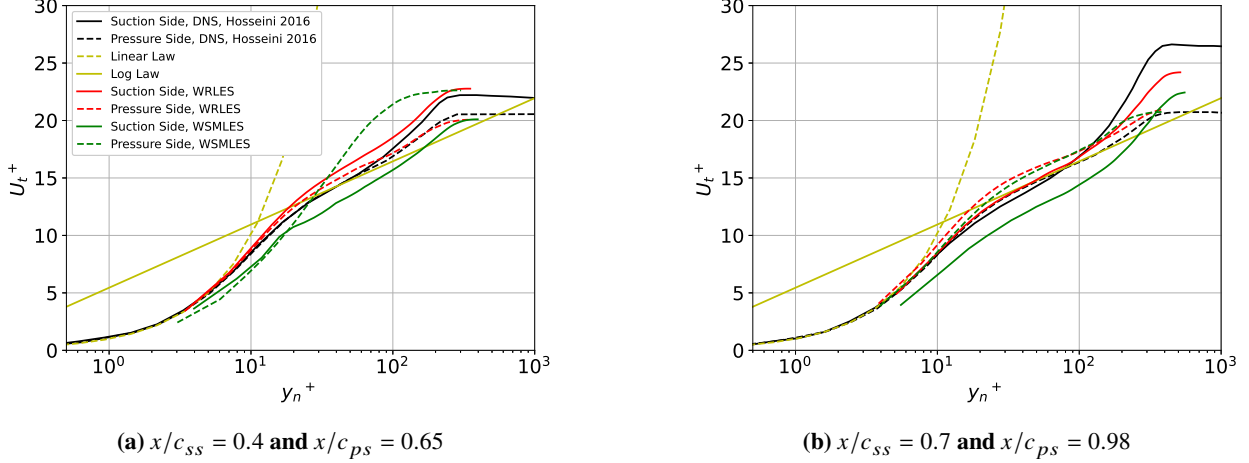


**Fig. 10 Comparison of boundary layer tangential velocity profiles at suction and pressure sides between WRLES, WSMLES and reference DNS.**

##### 5. Comparison of wall-pressure spectra

Since the development of the boundary layer on the airfoil is different in both the WRLES and WSMLES computations, the resulting wall pressure spectrum at the trailing edge can only be compared qualitatively after non-dimensionalization. The wall-pressure spectra in the vicinity of the suction-side trailing edge at chordwise positions  $x/c = 0.94, 0.96, 0.98$  are shown in Figure 11. The non-dimensionalization here is in terms of the wall variables. In the figures,  $\phi(\omega)$  refers to the one-sided dimensional wall-pressure spectrum and  $\delta_{99}$  is the 99% boundary layer thickness. The spectra predicted by the WRLES simulation are physical in nature as they follow the -5 slope at the high frequencies. Only a small part of the spectra follows the -1 scaling; this is deemed typical by Blake [19] as it corresponds to contributions from the scales in the log-law region, whose extent is not significant in the present simulations as the friction Reynolds number in the simulations in both WRLES and WSMLES is between 400 and 550 in the vicinity of the trailing edge. Although the shape of the spectra for the WSMLES follows that of the WRLES simulation, a significant level of spurious noise is found at high-frequencies. Whether these fluctuations arise from tripping or from the numerics is yet to be ascertained.

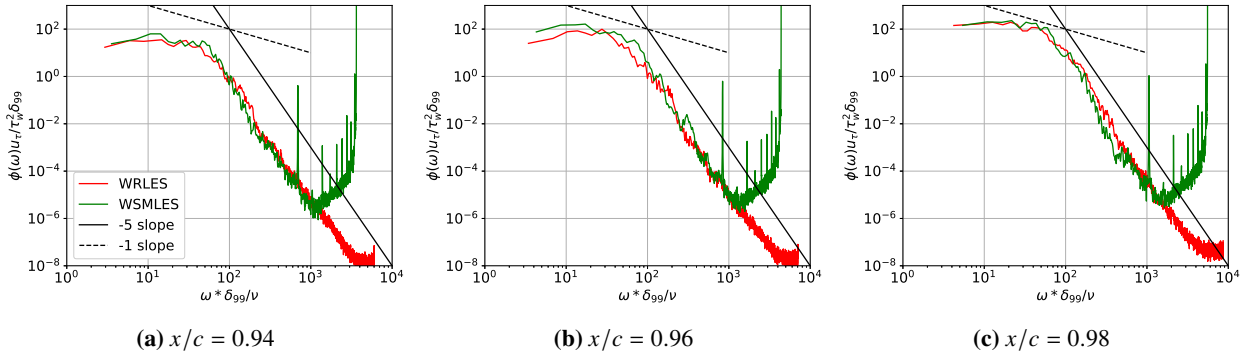


**Fig. 11 Non-dimensional frequency spectra of the wall-pressure fluctuations for the WRLES and WSMLES computations.**

## IV. Conclusions

The validation of the high-fidelity turbulence modelling approaches in EllipSys3D is conducted by comparing the data from channel flow simulations against that from DNS; this is done to not only elucidate the correctness of implementation but also evaluate their applicability to simulate wall-bounded flows. In this regard, the plots of mean flow profiles, turbulent stresses and two-point correlations for the channel flow test case are comparable to that of the DNS reference, indicating that the approaches are applicable to wall-bounded flows. Furthermore, the aerodynamic validation exercise of the airfoil test case by comparing the near-field flow solution against the DNS reference data shows that the current WRLES setup is capable of providing practicable results for a precursor CFD simulation in the context of hybrid CFD-CAA approaches. However, the computational resources required for using such methods render it impractical for the investigation of the flow physics behind the TE noise generation at high-Reynolds numbers. In this regard, approaches that model the inner part of the boundary layer which do not entail noise-producing turbulence are essential. One such approach used here to investigate the effect of wall-modelling on the wall-pressure spectra (and thus, TBL-TE noise) is the LES approach coupled with an algebraic wall stress model based on the Reichardt's log-law model.

Further tuning of the simulation parameters is required in the current WSMLES study to render the approach applicable to the precursor CFD simulations, which form a vital part of any high-fidelity hybrid CFD-CAA framework. The physical accuracy of the near-field flow solution is crucial as it will be coupled with an acoustics solver to obtain accurate far-field noise predictions. The acoustics solver will be developed and validated, the scope of which is the subject of a follow-up study. Furthermore, the wall-modelling capability of SST-IDDES [36] will also be evaluated in this context.

## References

- [1] Oerlemans, S., Sijtsma, P., and Méndez López, B., “Location and quantification of noise sources on a wind turbine,” *Journal of Sound and Vibration*, Vol. 299, No. 4-5, 2007, p. 869 – 883. <https://doi.org/10.1016/j.jsv.2006.07.032>, URL <https://www.scopus.com/inward/record.uri?eid=2-s2.0-33751108552&doi=10.1016%2fjsv.2006.07.032&partnerID=40&md5=5654f7d83dfa6e7f2c67df621fc8211b>.
- [2] Oerlemans, S., *Wind Turbine Noise Mitigation*, Springer International Publishing, Cham, 2022, pp. 1447–1462. [https://doi.org/10.1007/978-3-030-31307-4\\_73](https://doi.org/10.1007/978-3-030-31307-4_73), URL [https://doi.org/10.1007/978-3-030-31307-4\\_73](https://doi.org/10.1007/978-3-030-31307-4_73).
- [3] Williams, J. E., and Hall, L. H., “Aerodynamic sound generation by turbulent flow in the vicinity of a scattering half plane,” *Journal of Fluid Mechanics*, Vol. 40, 1970, pp. 657–670. <https://doi.org/10.1017/S0022112070000368>.
- [4] Amiet, R. K., “Acoustic radiation from an airfoil in a turbulent stream,” *Journal of Sound and Vibration*, Vol. 41, 1975, pp. 407–420. [https://doi.org/10.1016/S0022-460X\(75\)80105-2](https://doi.org/10.1016/S0022-460X(75)80105-2), URL <https://www.sciencedirect.com/science/article/pii/S0022460X75801052>.
- [5] Brooks, T. F., Pope, D. S., and Marcolini, M. A., “Airfoil self-noise and prediction,” , 7 1989. URL <https://ntrs.nasa.gov/citations/19890016302>.
- [6] Parchen, R. R., “Progress report DRAW: A prediction scheme for trailing edge noise based on detailed boundary layer characteristics,” Tech. rep., TNO Institute of Applied Physics, 1998.
- [7] Shen, W. Z., and Nørkær Sørensen, J., “Aeroacoustic modeling of turbulent airfoil flows,” *AIAA Journal*, Vol. 39, No. 6, 2001, p. 1057 – 1064. <https://doi.org/10.2514/2.1446>, URL <https://www.scopus.com/inward/record.uri?eid=2-s2.0-0035368194&doi=10.2514%2f2.1446&partnerID=40&md5=56dd3d97ff5ddb31f047e2bade6b4272>.
- [8] Seo, J.-H., and Moon, Y. J., “Perturbed compressible equations for aeroacoustic noise prediction at low Mach numbers,” *AIAA Journal*, Vol. 43, No. 8, 2005, p. 1716 – 1724. <https://doi.org/10.2514/1.3001>, URL <https://www.scopus.com/inward/record.uri?eid=2-s2.0-24144483166&doi=10.2514%2f1.3001&partnerID=40&md5=33196672d1497e15062d7a043ada6a70>.
- [9] Lighthill, M., “On Sound Generated Aerodynamically .1. General Theory,” *Proceedings Of The Royal Society Of London Series A-Mathematical and Physical Sciences*, Vol. 211, No. 1107, 1952, pp. 564–587. <https://doi.org/10.1098/rspa.1952.0060>.
- [10] Curle, N., “The influence of solid boundaries upon aerodynamic sound,” *Proceedings Of The Royal Society Of London Series A-Mathematical and Physical Sciences*, Vol. 231, No. 1187, 1955, pp. 505–514. <https://doi.org/10.1098/rspa.1955.0191>.
- [11] Ffwocs Williams, J., and Hawkings, D., “Sound Generation by Turbulence and Surfaces in Arbitrary Motion,” *Roy Soc London-Philosophical Trans Ser A*, Vol. 264, No. 1151, 1969, p. 321 – 342. URL <https://www.scopus.com/inward/record.uri?eid=2-s2.0-0014667963&partnerID=40&md5=606e6fa70da8f64dc831726bc29abcf>.

- [12] Farassat, F., “Derivation of Formulations 1 and 1A of Farassat,” , 3 2007. URL <https://ntrs.nasa.gov/citations/20070010579>.
- [13] Kirkup, S., “The boundary element method in acoustics: A survey,” *Applied Sciences*, Vol. 9, No. 8, 2019. <https://doi.org/10.3390/app9081642>, URL <https://www.scopus.com/inward/record.uri?eid=2-s2.0-85067105617&doi=10.3390%2fapp9081642&partnerID=40&md5=6689f6ba8e5ab0702713071dad8cacda>.
- [14] Shen, W. Z., Zhu, W., and Sørensen, J. N., “Aeroacoustic computations for turbulent airfoil flows,” *AIAA Journal*, Vol. 47, No. 6, 2009, p. 1518 – 1527. <https://doi.org/10.2514/1.40399>, URL <https://www.scopus.com/inward/record.uri?eid=2-s2.0-67650911897&doi=10.2514%2f1.40399&partnerID=40&md5=e53adfc4eb7c9a58d65898c4216b3dc3>.
- [15] Tenaud, C., Pellerin, S., Dulieu, A., and Ta Phuoc, L., “Large Eddy Simulations of a spatially developing incompressible 3D mixing layer using the  $v-\omega$  formulation,” *Computers & Fluids*, Vol. 34, No. 1, 2005, pp. 67–96. <https://doi.org/https://doi.org/10.1016/j.compfluid.2004.03.003>, URL <https://www.sciencedirect.com/science/article/pii/S0045793004000489>.
- [16] Wang, M., Moreau, S., Iaccarino, G., and Rogers, M., “LES prediction of wall-pressure fluctuations and noise of a low-speed airfoil,” *International Journal of Aeroacoustics*, Vol. 8, No. 3, 2009, pp. 177–197. <https://doi.org/10.1260/147547208786940017>.
- [17] Lilly, D. K., “A proposed modification of the Germano subgrid-scale closure method,” *Physics of Fluids A: Fluid Dynamics*, Vol. 4, No. 3, 1992, pp. 633–635. <https://doi.org/10.1063/1.858280>, URL <https://doi.org/10.1063/1.858280>.
- [18] Wolf, W. R., Azevedo, J. L. F., and Lele, S. K., “Convective effects and the role of quadrupole sources for aerofoil aeroacoustics,” *Journal of Fluid Mechanics*, Vol. 708, 2012, p. 502–538. <https://doi.org/10.1017/jfm.2012.327>.
- [19] Blake, W. K., *Mechanics of Flow-Induced Sound and Vibration: General Concepts and Elementary Sources: Second Edition*, Vol. 1, 2017. URL <https://www.scopus.com/inward/record.uri?eid=2-s2.0-85054122843&partnerID=40&md5=aa9b9ac52bae1944bc16a8f49568d183>.
- [20] Kocheemoolayil, J. G., and Lele, S. K., “Large eddy simulation of airfoil self-noise at high reynolds number,” *22nd AIAA/CEAS Aeroacoustics Conference, 2016*, 2016. <https://doi.org/10.2514/6.2016-2919>, URL <https://www.scopus.com/inward/record.uri?eid=2-s2.0-85057294446&doi=10.2514%2f6.2016-2919&partnerID=40&md5=91ab8cdcc2b48d55fbbb5cc6dc99d812>.
- [21] Sørensen, N., “General purpose flow solver applied to flow over hills,” Ph.D. thesis, 1995. Published 2003.
- [22] Moser, R. D., Kim, J., and Mansour, N. N., “Direct numerical simulation of turbulent channel flow up to  $Re_\tau = 590$ ,” *Physics of Fluids*, Vol. 11, No. 4, 1999, p. 943 – 945. <https://doi.org/10.1063/1.869966>.
- [23] Hosseini, S., Vinuesa, R., Schlatter, P., Hanifi, A., and Henningson, D., “Direct numerical simulation of the flow around a wing section at moderate Reynolds number,” *International Journal of Heat and Fluid Flow*, Vol. 61, 2016, p. 117 – 128. <https://doi.org/10.1016/j.ijheatfluidflow.2016.02.001>, URL <https://www.scopus.com/inward/record.uri?eid=2-s2.0-84961782297&doi=10.1016%2fj.ijheatfluidflow.2016.02.001&partnerID=40&md5=0b166ace06c2da9b63708cd4ff1d2c61>.
- [24] Plaza, G. V., Fischer, A., Lylloff, O., Bak, C., Olsen, A. S., Bertagnolio, F., Luesutthiviboon, S., Pereira, T. L., Ragni, D., Avallone, F., Suryadi, A., and Herr, M., “Benchmarking of the NACA 633-018 Trailing-Edge Noise in a Broad Reynolds Number Range as Part of the IEA Task 39,” *28th AIAA/CEAS Aeroacoustics Conference, 2022*, 2022. <https://doi.org/10.2514/6.2022-2981>, URL <https://www.scopus.com/inward/record.uri?eid=2-s2.0-85135086026&doi=10.2514%2f6.2022-2981&partnerID=40&md5=7f9007a8d6f90aafae25953f871236ed>.
- [25] Lyu, B., Azarpeyvand, M., and Sinayoko, S., “Prediction of noise from serrated trailing edges,” *Journal of Fluid Mechanics*, Vol. 793, 2016, p. 556 – 588. <https://doi.org/10.1017/jfm.2016.132>, URL <https://www.scopus.com/inward/record.uri?eid=2-s2.0-84962570382&doi=10.1017%2fjfm.2016.132&partnerID=40&md5=2a308e6121b45704c8dd04fee6aed4f2>.
- [26] Fischer, A., Bertagnolio, F., Shen, W. Z., and Madsen, J., “Noise model for serrated trailing edges compared to wind tunnel measurements,” *Journal of Physics: Conference Series*, Vol. 753, No. 2, 2016. <https://doi.org/10.1088/1742-6596/753/2/022053>, URL <https://www.scopus.com/inward/record.uri?eid=2-s2.0-84995526975&doi=10.1088%2f1742-6596%2f753%2f2%2f022053&partnerID=40&md5=50775a471cfc6537101b90acc0c7645b>.
- [27] Michelsen, J. A., “Basis3D - a Platform for Development of Multiblock PDE Solvers,” *Technical Report AFM 92-05, Department of Fluid Mechanics, Technical University of Denmark*, 1992.
- [28] Michelsen, J. A., “Block structured Multigrid solution of 2D and 3D elliptic PDE’s,” *Technical Report AFM 94-06, Department of Fluid Mechanics, Technical University of Denmark*, 1994.
- [29] Nicoud, F., and Ducros, F., “Subgrid-scale stress modelling based on the square of the velocity gradient tensor,” *Flow, Turbulence and Combustion*, Vol. 62, 1999, p. 183 – 200. <https://doi.org/10.1023/A:1009995426001>.

- [30] Reichardt, H., “Vollständige Darstellung der turbulenten Geschwindigkeitsverteilung in glatten Leitungen,” *ZAMM - Journal of Applied Mathematics and Mechanics / Zeitschrift für Angewandte Mathematik und Mechanik*, Vol. 31, No. 7, 1951, pp. 208–219. <https://doi.org/10.1002/zamm.19510310704>, URL <https://onlinelibrary.wiley.com/doi/abs/10.1002/zamm.19510310704>.
- [31] Schlatter, P., and Örlü, R., “Turbulent boundary layers at moderate Reynolds numbers: inflow length and tripping effects,” *Journal of Fluid Mechanics*, Vol. 710, 2012, p. 5–34. <https://doi.org/10.1017/jfm.2012.324>.
- [32] CHOI, H., and MOIN, P., “EFFECTS OF THE COMPUTATIONAL TIME-STEP ON NUMERICAL-SOLUTIONS OF TURBULENT-FLOW,” *JOURNAL OF COMPUTATIONAL PHYSICS*, Vol. 113, No. 1, 1994, pp. 1–4. <https://doi.org/10.1006/jcph.1994.1112>.
- [33] Schoppa, W., and Hussain, F., “Coherent structure dynamics in near-wall turbulence,” *FLUID DYNAMICS RESEARCH*, Vol. 26, No. 2, 2000, pp. 119–139. [https://doi.org/10.1016/S0169-5983\(99\)00018-0](https://doi.org/10.1016/S0169-5983(99)00018-0).
- [34] Olesen, P. J., Hodžić, A., Andersen, S. J., Sørensen, N. N., and Velte, C. M., “Dissipation-optimized proper orthogonal decomposition,” *Physics of Fluids*, Vol. 35, No. 1, 2023. <https://doi.org/10.1063/5.0131923>, 015131.
- [35] Sørensen, N., *HypGrid2D a 2-D mesh generator*, No. 1035(EN) in Denmark. Forskningscenter Risoe. Risoe-R, 1998.
- [36] Gritskevich, M. S., Garbaruk, A. V., Schütze, J., and Menter, F. R., “Development of DDES and IDDES formulations for the  $k-\omega$  shear stress transport model,” *Flow, Turbulence and Combustion*, Vol. 88, 2012. <https://doi.org/10.1007/s10494-011-9378-4>.